

FREQUENCY MODULATION OF DIRECTLY IMAGED EXOPLANETS: GEOMETRIC EFFECT AS A PROBE OF PLANETARY OBLIQUITY

HAJIME KAWAHARA^{1,2}

Submitted on Feb.3, 2016; Accepted on Mar.9, 2016

ABSTRACT

We consider the time-frequency analysis of a scattered light curve by a directly imaged exoplanet. We show that the geometric effect due to planetary obliquity and orbital inclination induce the frequency modulation of the apparent diurnal periodicity. We construct a model of the frequency modulation and compare with the instantaneous frequency extracted from the pseudo-Wigner distribution of the simulated light curves of a cloudless Earth. The model provides good agreement with the simulated modulation factor even for the light curve with Gaussian noise comparable to the signal. Notably, the shape of the instantaneous frequency is sensitive to the difference between prograde, retrograde, and pole-on spin rotations. Whereas our technique requires the static property of the albedo map, it does not need to solve the albedo map of the planet. The time-frequency analysis is complementary to other methods which utilize the amplitude modulation. This paper demonstrates the importance of the frequency domain of the photometric variability to the characterization of directly imaged exoplanet in future.

Subject headings: astrobiology – Earth – scattering – techniques: photometric

1. INTRODUCTION

Photometric variability of scattered light has been considered as an important probe to characterize directly imaged exoplanets in near future. In the context of the habitable planet search, Ford et al. (2001) demonstrated that inhomogeneous clouds and surface components of Earth generate photometric variability due to a spin rotation. Inversion techniques of the surface distribution have been extensively studied (e.g. Cowan et al. 2009; Oakley & Cash 2009; Fujii et al. 2010; Kawahara & Fujii 2010; Cowan et al. 2011; Fujii et al. 2011; Kawahara & Fujii 2011; Fujii & Kawahara 2012).

The inversion method using the diurnal and annual variability, dubbed the spin-orbit tomography, retrieves not only the two-dimensional surface distribution but also the planet obliquity (Kawahara & Fujii 2010, 2011; Fujii & Kawahara 2012). The planet obliquity (axial tilt) is the important parameter for exoplanet's environment (e.g. Williams & Kasting 1997; Williams & Pollard 2003) and formation theory (e.g. Agnor et al. 1999; Chambers 2001; Kokubo & Ida 2007) but has not yet been measured. Several observational features, other than the photometric variability, have been proposed as a probe of the obliquity including the difference between the ingress and egress shapes in a transit curve (Seager & Hui 2002; Barnes & Fortney 2003; Carter & Winn 2010), the modulation of the planet's radial velocity (Kawahara 2012), the Rossiter-McLaurin effect at planet's occultation (Nikolov & Sainsbury-Martinez 2015).

In the framework of the spin-orbit tomography, the obliquity is simultaneously derived from the retrieval

of the surface map (Kawahara & Fujii 2010, 2011; Fujii & Kawahara 2012). The generality of the obliquity retrieval from the photometric variation has been studied recently by Schwartz et al. (2015). They explained how the obliquity affected the shape and location of the kernel of the scattered light. In essence, these methods use information on the amplitude modulation to extract the spin information. Hence, the albedo map of the planet contributes nuisance parameters to the global light curve fit. In this paper, we focus on the frequency domain of the photometric variability, rather than the amplitude modulation. We utilize the frequency modulation as an estimator of the obliquity, which is less sensitive to the albedo distribution of the planet.

Regarding the photometric variability in the frequency domain, Pallé et al. (2008) presented a pioneering work applying the autocorrelation function to the simulated photometric variation. They showed that the photometric variation of the simulated Earth contains sufficient information to measure the spin rotation period despite variable weather pattern. Visser & van de Bult (2015) studied the Fourier coefficient of the photometric variation for various surface types of Earth-like planets and several configurations (i.e. obliquity and inclination). The Fourier analysis of the reflected light curve has also been used in the field of asteroids (e.g. Russell 1906; Barucci et al. 1989). We extend the frequency analysis of the photometric variability to the time-frequency analysis to consider the frequency modulation. We show that both the orientation of the spin axis and the orbital inclination modulate the frequency of the apparent variability of the scattered light. In this paper, we concentrate on the geometric effect of the frequency modulation and restrict the scope of targets to the scattered light by the static planetary surface.

The rest of the paper is organized as follows. In Section 2, we construct a simple model of the frequency modulation due to the geometric effect. In Section 3, we simulate

Electronic address: kawahara@eps.s.u-tokyo.ac.jp

¹ Department of Earth and Planetary Science, The University of Tokyo, Tokyo 113-0033, Japan

² Research Center for the Early Universe, School of Science, The University of Tokyo, Tokyo 113-0033, Japan

the photometric variability assuming the Lambert model of the static albedo distribution. We extract the instantaneous frequency from the pseudo-Wigner distribution of the simulated light curve. We discuss the other effects that cause the frequency modulation in Section 4. We also compare our results with the spin-orbit tomography. In Section 5, we summarize our findings.

2. APPARENT DIURNAL PERIODICITY

Let us first consider a prograde rotation of an aligned planet with a static surface distribution. The spin rotation frequency is defined by $f_{\text{spin}} = 1/P_{\text{spin}}$, where P_{spin} is the sidereal day of the planet (the spin rotation period). The sidereal day is the period that it takes the planet to make one rotation about the inertial reference frame of the stellar system. The period of the photometric variation is identical to the so-called synodic day defined as the period that it takes to rotate once around the central star. Then, the apparent diurnal periodicity derived from the photometric variability is $f_{\text{obs}} = f_{\text{spin}} - f_{\text{orb}}$, where $f_{\text{orb}} = 1/P_{\text{orb}}$ is the orbital frequency and P_{orb} is the orbital period. For the retrograde rotation (the obliquity of 180°), we obtain $f_{\text{obs}} = f_{\text{spin}} + f_{\text{orb}}$. The question is how the obliquity changes the apparent diurnal periodicity.

Figure 1 illustratively explains how the obliquity and the orbital inclination induce the frequency modulation. The Panel (a) displays prograde, retrograde, and pole-on planets in a face-on orbit. The illuminated area painted by white moves in the direction of the red arrow. Because the rotation axis of the illuminated area is aligned with the spin axis, the photometric frequency of the prograde and retrograde planets is stationarily shifted as $f_{\text{obs}} = f_{\text{spin}} \pm f_{\text{orb}}$. For the case of the pole-on planets, the rotation axis of the illuminated area is not aligned with the spin axis. In the panel (b), the representative point (the weighted center) of the illuminated area is indicated by a filled cross. When the latitude of the weighted center moves from the center (I) to left (II), the apparent rotation speeds up. The shift of the weighted center to right decelerates the apparent rotation (III). Thus, the motion of the illuminated area modulates the frequency of the apparent rotation.

The motion of the illuminated area due to the orbital inclination also induces the frequency modulation by the same principle. As shown in the panel (c), the shift of the illuminated area around the inferior conjunction negatively modulates the apparent rotation rate. In general, the frequency modulation due to the orbital inclination is significant near the inferior conjunction. We call these types of the frequency modulation the geometric frequency modulation.

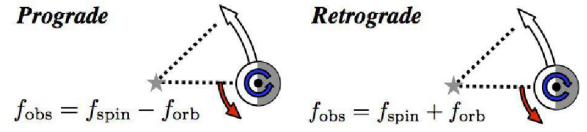
2.1. Maximum Weighted Longitude Approximation of the Synodic Diurnal Modulation

The apparent periodicity depends on both the spin vector and the albedo distribution. The integrated light from the Lambert surface is expressed as (Kawahara & Fujii 2010)

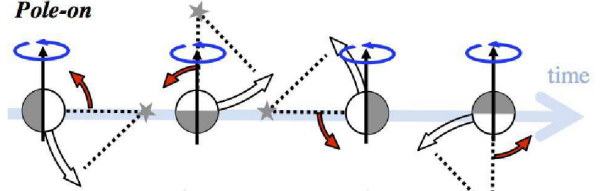
$$I_b \propto \int_S a(\phi, \theta) W_V(\phi, \theta) W_I(\phi, \theta) \sin \theta d\theta d\phi, \quad (1)$$

where $a(\phi, \theta)$ is the albedo distribution on the planetary surface of (ϕ, θ) , S is the illuminated and visible area,

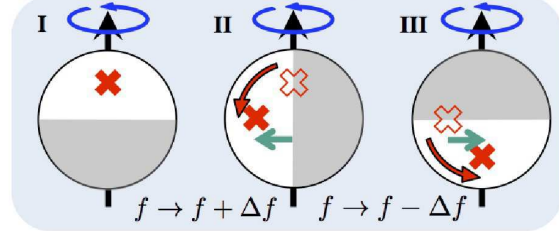
(a) Face-on orbit



Pole-on



(b) Zoom-up



(c) Edge-on orbit & prograde planet

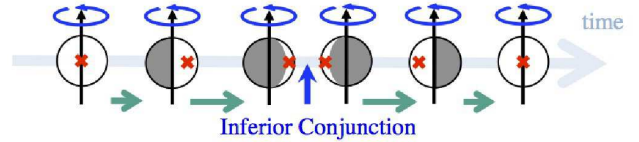


Figure 1. Schematic explanation of the geometric frequency modulation. The star mark indicates the position of a central star. The black and white arrows are the spin axis vector of the planet and the direction of the orbital motion. The red arrows indicate a direction of the shift of the illuminated area painted by white. The configurations for prograde, retrograde and the pole-on rotations are shown in the panel (a). The panel (b) shows an enlarged view of the pole-on case. The filled cross shows the weighted center of scattered light. According to the orbital motion, the longitude of the weighed center moves on a planet's disk as indicated by the green arrow. The apparent rotation is accelerated or decelerated by the motion of the weighted center. The panel (c) explains the frequency modulation induced by the orbital inclination. See the text for the details.

$W_V(\phi, \theta) = \mathbf{e}_O \cdot \mathbf{e}_R$ and $W_I(\phi, \theta) = \mathbf{e}_S \cdot \mathbf{e}_R$ are the weight functions of the visible and illuminated areas and \mathbf{e}_S , \mathbf{e}_O and \mathbf{e}_R are the unit vectors of \vec{p}_S , \vec{p}_O (p =the planet center, s =the stellar center, and o =the observer) and, the normal vector of the surface.

It is useful to exclude the influence of albedo distribution from a model. Assuming that the surface at the maximum weighted longitude mainly attributes the variability, we construct a model of photometric periodicity by computing the phase shift of the maximum weighted longitude, $\hat{\phi}_M$. If the spin axis is aligned with the orbital axis, i.e., the planetary obliquity ζ is zero, $\hat{\phi}_M$ moves according to the spin rotation. Then we obtain $\hat{\phi}_M = -\Phi$, where Φ is the diurnal phase of spin rotation defined by $\Phi = f_{\text{spin}} t / 2\pi$. The minus sign implies that the sun rises from the east and sets in the west.

The orbital motion modulates $\hat{\phi}_M$ for the non-zero obliquity. The instantaneous frequency of the periodicity

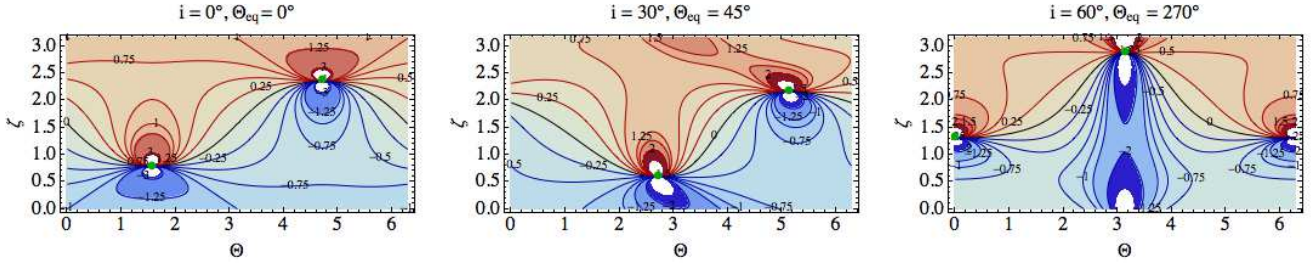


Figure 2. Examples of the modulation factor under the maximum weighted longitude approximation, $\epsilon_\zeta(\Theta)$. We assume $(i = 0^\circ, \Theta_{\text{eq}} = 0^\circ)$, $(i = 30^\circ, \Theta_{\text{eq}} = 45^\circ)$, and $(i = 60^\circ, \Theta_{\text{eq}} = 270^\circ)$ from left to right. The singular points are marked by the green points.

at the maximum weighted longitude is given by

$$f_{\text{obs}} = -\frac{1}{2\pi} \frac{\partial \hat{\phi}_M}{\partial t} = -\frac{\partial \hat{\phi}_M}{\partial \Theta} f_{\text{orb}}, \quad (2)$$

where $\Theta = f_{\text{orb}} t / 2\pi$ is the orbital phase. Using the relation,

$$\frac{\partial(\hat{\phi}_M + \Phi)}{\partial \Theta} = \frac{\partial \hat{\phi}_M}{\partial \Theta} + \frac{\partial \Phi}{\partial \Theta} = \frac{\partial \hat{\phi}_M}{\partial \Theta} + \frac{f_{\text{spin}}}{f_{\text{orb}}}$$

we rewrite equation (2) as

$$f_{\text{obs}} = f_{\text{spin}} + \epsilon_\zeta(\Theta) f_{\text{orb}}, \quad (3)$$

where we define the modulation factor

$$\epsilon_\zeta(\Theta) \equiv -\frac{\partial(\hat{\phi}_M + \Phi)}{\partial \Theta} = -\frac{\kappa'(\Theta)}{1 + \kappa(\Theta)^2}, \quad (4)$$

$$\kappa(\Theta) \equiv \tan(\hat{\phi}_M + \Phi). \quad (5)$$

To compute $\kappa(\Theta)$, we use the inertia coordinate system described in Fujii & Kawahara (2012).

$$\mathbf{e}_S = (\cos(\Theta - \Theta_{\text{eq}}), \sin(\Theta - \Theta_{\text{eq}}), 0)^\top, \quad (6)$$

$$\mathbf{e}_O = (\sin i \cos \Theta_{\text{eq}}, \sin i \sin \Theta_{\text{eq}}, \cos i)^\top, \quad (7)$$

where Θ_{eq} is the orbital phase at equinox. Because W_I and W_V are the inner products, $\mathbf{e}_O \cdot \mathbf{e}_R$ and $\mathbf{e}_S \cdot \mathbf{e}_R$, \mathbf{e}_R has the maximum weight when $\mathbf{e}_O \cdot \mathbf{e}_R = \mathbf{e}_S \cdot \mathbf{e}_R$. Then, we obtain the vector from the center to the maximum weighted point as

$$\mathbf{e}_M = \frac{\mathbf{e}_S + \mathbf{e}_O}{|\mathbf{e}_S + \mathbf{e}_O|} \quad (8)$$

$$= \frac{1}{L} \begin{pmatrix} \cos(\Theta - \Theta_{\text{eq}}) + \cos \Theta_{\text{eq}} \sin i \\ \sin(\Theta - \Theta_{\text{eq}}) - \sin \Theta_{\text{eq}} \sin i \\ \cos i \end{pmatrix}, \quad (9)$$

where $L \equiv |\mathbf{e}_S + \mathbf{e}_O| = \sqrt{2 + 2 \cos \Theta \sin i}$.

We set the Cartesian coordinates fixed on the planetary surface $\mathbf{e}'_R(\phi, \theta) = (\cos \phi \sin \theta, \sin \phi \sin \theta, \cos \theta)^\top$. We call it the surface Cartesian coordinate. The spin vector is $\mathbf{e}'_{\text{spin}} = (0, 0, 1)^\top$ in the surface Cartesian coordinate. The conversion between the inertia coordinate \mathbf{e}_R and the surface Cartesian coordinate \mathbf{e}'_R is expressed as

$$\begin{aligned} \mathbf{e}_R &= R(\zeta) \hat{S}(\Phi) \mathbf{e}'_R(\phi, \theta) \\ &= R(\zeta) \mathbf{e}'_R(\phi + \Phi, \theta) \\ &= \begin{pmatrix} \cos(\phi + \Phi) \sin \theta \\ \cos \zeta \sin(\phi + \Phi) \sin \theta + \sin \zeta \cos \theta \\ \sin \zeta \sin(\phi + \Phi) \sin \theta - \cos \zeta \cos \theta \end{pmatrix}, \end{aligned} \quad (10)$$

where $R(\zeta)$ is the rotation matrix for the clockwise rotation around the x -axis and $\hat{S}(\Phi)$ is a rotation operator

of $\phi \rightarrow \phi + \Phi$. To describe \mathbf{e}_M in the surface Cartesian coordinate (ϕ_M, θ_M) , we multiply $R(-\zeta)$ by \mathbf{e}_M ,

$$\begin{aligned} \hat{S}(\Phi) \mathbf{e}'_M &\equiv R(-\zeta) \mathbf{e}_M. \\ &= \frac{1}{L} \begin{pmatrix} \cos(\Theta - \Theta_{\text{eq}}) + \cos \Theta_{\text{eq}} \sin i \\ \cos \zeta [\sin(\Theta - \Theta_{\text{eq}}) - \sin i \sin \Theta_{\text{eq}}] - \cos i \sin \zeta \\ \cos i \cos \zeta + \sin \zeta (\sin(\Theta - \Theta_{\text{eq}}) - \sin i \sin \Theta_{\text{eq}}) \end{pmatrix}, \end{aligned} \quad (11)$$

Dividing the y -component by the x -component, we obtain tangent of $\hat{\phi}_M + \Phi$,

$$\begin{aligned} \tan(\hat{\phi}_M + \Phi) &= \frac{\cos \zeta [\sin(\Theta - \Theta_{\text{eq}}) - \sin \Theta_{\text{eq}} \sin i] - \sin \zeta \cos i}{\cos(\Theta - \Theta_{\text{eq}}) + \cos \Theta_{\text{eq}} \sin i}. \end{aligned} \quad (13)$$

Substituting equation (13) and its derivative for $\kappa(\Theta)$ and $\kappa'(\Theta)$ in equation (4), we obtain the analytic forms of the modulation factor and the instantaneous frequency of the photometric variation in equation (3). The explicit form of equation (4) is given in Appendix A. Figure 2 displays several examples of a different geometry of the modulation factor of the maximum weighted longitude approximation. The green points indicate the singular points where the unit vector of the maximum weighted point is aligned with the spin vector $|\mathbf{e}'_M| = |\mathbf{e}'_{\text{spin}}|$ (see Appendix A for the derivation). On the singular point, the kernel of the scattered light $W_I(\phi, \theta)W_V(\phi, \theta)$ is over the spin vector, corresponding to the maximum point of the kernel width in Figure 3 (left) of Schwartz et al. (2015).

We can classify the instantaneous frequency curve into three domains; (A) $\zeta \leq \zeta_I$, (B) $\zeta_I < \zeta < \zeta_{II}$, and (C) $\zeta \geq \zeta_{II}$, where ζ_I and $\zeta_{II} (> \zeta_I)$ are the obliquity of the two singular points. In the domains A, B, and C, $\epsilon(\Theta)$ has one negative peak, one negative+one positive peaks, one positive peaks, respectively. For instance, we obtain $\zeta_I = \pi/4$ and $\zeta_{II} = 3\pi/4$ for a face-on orbit. Thus, the type of the geometric frequency modulation is sensitive to the difference between the prograde, pole-on, and retrograde spins, roughly corresponding to the domain A, B, and C.

In Figure 2, we only show one example of Θ_{eq} for each orbital inclination. However, the topological structure is determined by the position of the singular points and the null line ($\epsilon(\Theta, \zeta) = 0$) which connects the singular points. In the Appendix A, we explain the general properties of the singular points and the null lines in detail. Using these features, one can roughly reproduce the general trend of the modulation factor for arbitrary parameters.

3. EXTRACTING THE INSTANTANEOUS FREQUENCY FROM TIME-FREQUENCY REPRESENTATIONS

We compare equation (4) with the simulations of the rotational light curve whose planetary surface is stationary. We use a static cloud-subtracted Earth model. The static cloud-subtracted Earth is a toy model of the color-difference map proposed by Kawahara & Fujii (2011). In their paper, they showed that the spin-orbit tomography inferences of the obliquity using the light curve of the single band is poor because of the presence of clouds. The obliquity can be well retrieved from the color difference of the light curve (for instance $0.85 - 0.45 \mu\text{m}$) because the color difference of $0.85 - 0.45 \mu\text{m}$ efficiently suppresses the effect of clouds. The static cloud-subtracted Earth model as shown in Figure 3 has a zero albedo ocean and a constant albedo land after removing the cloud cover fraction. We use ISCCP D1 data (the cloud map in 2008/6/30 21:00) as the cloud cover fraction. The spherical pixelization is implemented using HealPix (Górski et al. 2005) with the total pixel number of 3072.

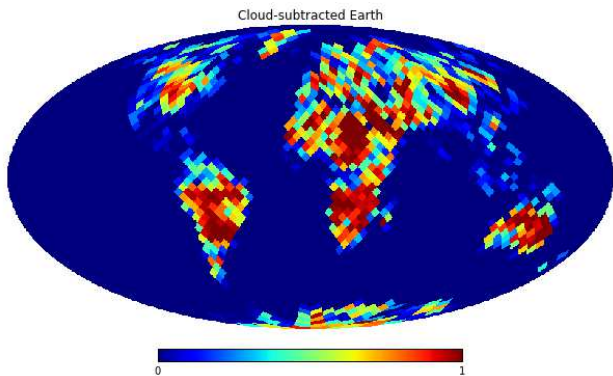


Figure 3. Static cloud-subtracted Earth (static cloud-subtracted Earth) model.

We set $N = 4096$ grids with the equal time interval (~ 2.1 hour) during a year and compute the mock photometric light curve using equations (1), (6), (7), and, (10). We adopt $P_{\text{spin}} = 23.9344699$ hour and $P_{\text{orb}} = 365.242190402$ day corresponding to the synodic day and a year of Earth. We add Gaussian noises with the standard deviation $\sigma_n = 0$ and σ_s , (100% noise) to the relative flux, where σ_s is the standard deviation of the photometric variation. Figure 4 shows examples of the generated light curve for the geometric parameter set, $\zeta = \pi/3$, $i = 0$ (face-on), and $\Theta_{\text{eq}} = \pi$.

We estimate the instantaneous frequency by extracting the ridge of the time-frequency representation that describes the signal in both time and frequency domains (e.g. Cohen 1995). We use the pseudo-Wigner distribution³ as the time-frequency representation. In Appendix B, we provide a detailed description of the pseudo-Wigner distribution as an instantaneous frequency estimator. We here provide a summary. The pseudo-Wigner

³ The Wigner distribution whose variable is an analytic signal of a real-valued signal is sometimes called the Wigner-Ville distribution (Boashash 2015).

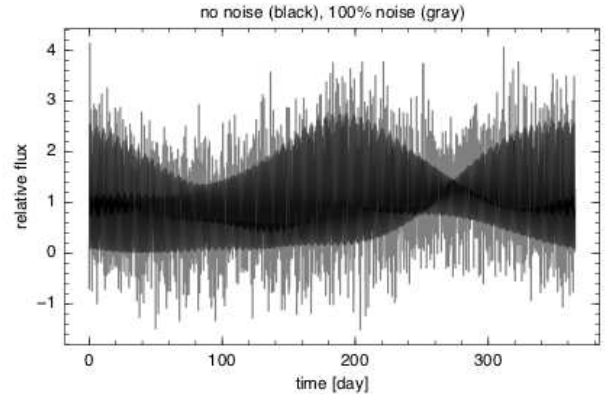


Figure 4. Simulated photometric variation with no noise (black), and 100 % noise (gray).

distribution is expressed as

$$g(f, t) = \int_{-\infty}^{\infty} h(\tau) z(t + \tau/2) z^*(t - \tau/2) e^{-2\pi i f \tau} d\tau, \quad (14)$$

where z and z^* are the analytic signal of the data and its conjugate, and $h(\tau)$ is the window. For the discrete sequence, $z[1], z[2], \dots, z[N]$

$$g(f, t_i) = \sum_{|m| < N/2} h[m] z[i + m] z^*[i - m] e^{-2\pi i f \tau} d\tau, \quad (15)$$

where $m = \min(i - 1, N - i)$. Using equation (15), we compute the time-frequency representation between $f_i = 0.96$ to $f_j = 1.05$ [1/day] around $f = 1/P_{\text{spin}}$. The ridge line of the time-frequency representation is interpreted as the instantaneous frequency,

$$\hat{f}(t) = \operatorname{argmax}_{[f_i, f_j]} g(f, t), \quad (16)$$

where $[f_i, f_j]$ is the frequency range of interest.

We translated the MATLAB code for computing equation (15) in the Time-Frequency Toolbox⁴ to Julia language (Bezanson et al. 2014). The fact that f is not necessarily discrete is important for our purpose because the frequency modulation is small (of the order of $\delta f/f \approx P_{\text{spin}}/P_{\text{orb}}$). Practically, the fast Fourier transform (FFT) is inefficient to explore the narrow frequency range of interest. We replaced the FFT in the original code by the non-uniform FFT algorithm (Greengard & Lee 2004). In Appendix C, we describe the implementation of the non-uniform FFT into the pseudo-Wigner distribution and the comparison of the systems with the non-uniform FFT and the FFT. We also test our code for known signals with a given instantaneous frequency in Appendices C and D. In practice, the selection of the window width of $h(\tau)$, w , is critical for noisy data. We adopt the window width $w = N/8$ for the 100 % noise. Our code used in the paper is publicly available under the GNU General Public Licence⁵.

The analytic signal $z[1], z[2], \dots, z[N]$ in equation (15) is generated by the following procedure. To remove the

⁴ <http://tftb.nongnu.org>

⁵ <https://github.com/HajimeKawahara/juwvid>

amplitude modulation (detrrending of the amplitude), we compute interpolation function of the mock photometric light curve of the mean and standard deviation for each set of 64 adjacent data points (\sim six days). We subtract the interpolated mean from the light curve and divide them by the interpolated standard deviation. This pre-processing enables us to exclude unnecessary amplitude modulations from the frequency analysis and normalizes the light curve. Then, we compute the analytic signal of the normalized light curve using the DSP package of Julia.

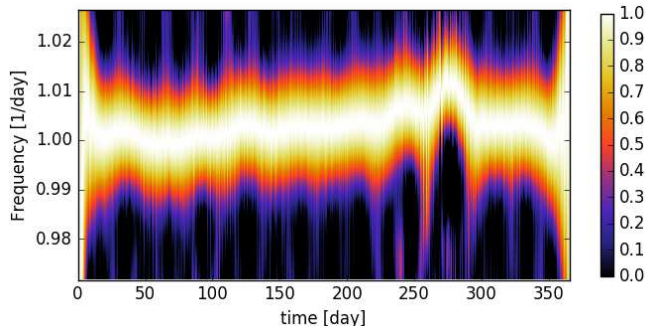


Figure 5. Time-frequency representation by the pseudo-Wigner distribution of the light curve with the 100 % noise

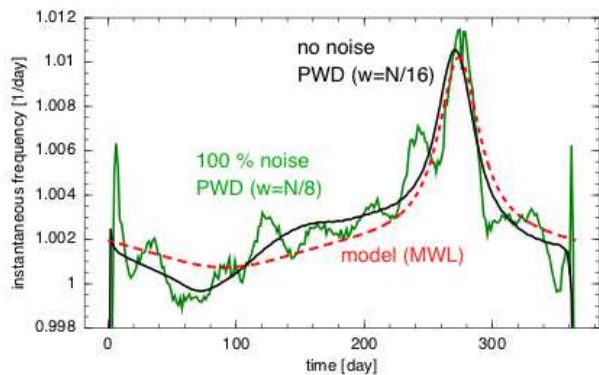


Figure 6. Estimated instantaneous frequencies by the pseudo-Wigner distribution (labeled as PWD) for the light curves with no noise (black) and 100 % noise (green). The dashed curve (red) is the theoretical prediction from the maximum weighted longitude approximation (labeled as MWL)

Figure 5 shows an example of the time-frequency representation of the 100 % noise case for $\zeta = 60^\circ$, $\Theta_{\text{eq}} = 180^\circ$, $i = 0^\circ$. Extracting the ridge line of the time-frequency representation, we extract the extracted instantaneous frequency shown by the green line in Figure 6. The black curve in Figure 6 is the extracted instantaneous frequencies of the light curve with no noise ($w = N/16$). The extracted instantaneous frequency of the 100 % noise still exhibits same characteristic features of the geometric effect to that of the noiseless case. The dashed line indicates the instantaneous frequency from the maximum weighted longitude approximation. The prediction curve from the maximum weighted longitude

approximation reproduces the general characteristics of the instantaneous frequency of the simulations. However, there remains some difference between the black and red lines. Because the test given in Appendix C does not exhibit such the difference (Figure 10), this difference originates from the influence of the albedo distribution we ignore in the maximum weighted longitude approximation.

We investigate other dozen parameter sets for ζ , Θ_{eq} . We confirmed that we can extract the instantaneous frequency for the $\sim 100\%$ noise in most cases, but, in some configurations, we need to decrease the noise level to $\sim 30\%$ to extract the instantaneous frequency. We also found the similar cases sometimes happen when randomly rotating the albedo distribution for the fiducial parameter set. We found that these noise sensitive cases are attributed to the particular configurations that prevent enough amplitude of the photometric variation depending on the albedo distribution and the geometric parameters. Because pursuing the optimization to noise is beyond the scope of our paper, we do not try to improve further to detect the instantaneous frequency for these noise sensitive cases. Instead, we point out that numerous techniques in the high noise environment have been proposed (see Stankovic et al. 2013; Boashash 2015). These techniques will potentially improve the detectability for the noise-sensitive configurations.

3.1. Comparison with the maximum weighted longitude model

Figure 7 displays the modulation factor of the simulated light curve derived from the pseudo-Wigner distribution. We used the light curves with no noise, adopted the pseudo-Wigner distribution with the window width $w = N/16$ to suppress the bias (see Appendix D). Comparing with Figure 2, we find that the maximum weighted longitude approximation provides a close agreement with the simulated modulation factor in spite of ignoring the dependence of the albedo distribution of the frequency modulation. Thus, the frequency modulation contains sufficient information on the obliquity.

For the highly inclined case ($i \gtrsim 60^\circ$), the intensity of the light curve significantly decreases near the inferior conjunction, and the gradient of the light curve also increases. These disadvantages near the inferior conjunction prevent accurate measurements of the frequency modulation due to the orbital inclination. Even for $i = 60^\circ$ (the right panel in Figure 7), one can see the disturbance of the extracted instantaneous frequency near the inferior conjunction $\Theta = \pi$. However, the difficulty for highly inclined planets is less problematic for our purpose because the direct imaging at inferior conjunction for highly inclined planets is challenging in the first place.

To use the instantaneous frequency as an obliquity estimator, we fit the extracted instantaneous frequency by the maximum weighted longitude model. We generate 1000 realizations of the light curves with the noise for each parameter set and extract the instantaneous frequencies by the pseudo-Wigner distribution ($w = N/8$). We fit them by the maximum weighted longitude approximation using the Levenberg-Marquardt algorithm (mpfit Markwardt 2009). We regard P_{orb} and i as known parameters because the monitoring observation of the

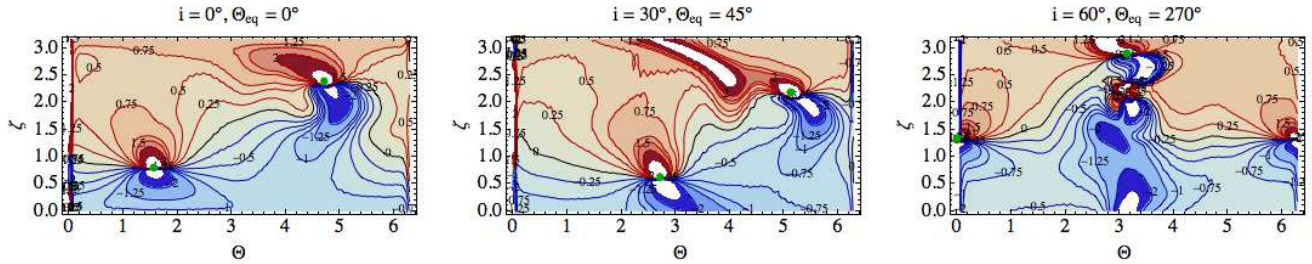


Figure 7. Examples of the simulated modulation factor using the pseudo-Wigner distribution, corresponding to the panels in Figure 2.

direct imaging provides them. Then, there remain the three free parameters ζ , Θ_{eq} , and the spin rotation period. To avoid the aliasing effect, we exclude the most left and most right ~ 19 days of the extracted instantaneous frequency.

Figure 8 (top) shows the areas enclosing 68 and 95 % of the best-fit obliquity and phase. We assume a face-on orbit and $\Theta_{\text{eq}} = 180^\circ$ and test three different obliquities, A: $\zeta = 60^\circ$, B: $\zeta = 23^\circ$, and C: $\zeta = 157^\circ$. For the case A and B, we set the 100 % noise, but, we reduce the noise to 30 % for the case C because the case C is the noise-sensitive configuration. The points mark the input values. The estimated planetary obliquity and the estimated phase are in good agreements with the input values for the cases A and B, although there are slight shifts of the center from the input. For the case C, the bias is much larger than the statistical uncertainty. This bias is due to lack of the albedo information in the maximum weighted longitude approximation. Although the maximum weighted longitude approximation (Fig 2) roughly reproduces the simulated modulation factor (Fig 7), the peak positions for a given ζ between Figures 2 and 7 often differs several ten degree in Θ_{eq} . This difference also impacts on the uncertainty of the obliquity. Considering these facts, the confidence region of the fitting with the maximum weighted longitude approximation is typically $\Delta\zeta \sim 20^\circ$ and $\Delta\Theta_{\text{eq}} \sim 45^\circ$, as shown by the yellow cross. To further reduce the bias, one requires the modeling of the albedo distribution in the instantaneous frequency model. We do not consider the albedo modeling in this paper.

The uncertainty of the spin rotation frequency relies on the determination of the offset of the instantaneous frequency. As shown in the bottom panel of Figure 8, the best-fit spin rotation frequency agrees with the input one in $\sim 0.02 - 0.03$ % accuracy, corresponding to a few hours error during one year.

4. DISCUSSION

4.1. Light travel time effect

The finite light-travel time effect known as Rømer delay also induces the frequency modulation. The light-travel time effect provides direct information on the length of the system. The light-travel time effect has been detected in the forms of the modulation of the eclipse timing of the hierarchical triple-star systems (Rappaport et al. 2013; Conroy et al. 2014; Masuda et al. 2015; Borkovits et al. 2016) and the time delay between a transit and a secondary eclipse of exoplanets (Agol et al. 2010). Pulsating stars are also used as a clock to measure the frequency modulation (Shibahashi & Kurtz 2012). Here, we consider the light-

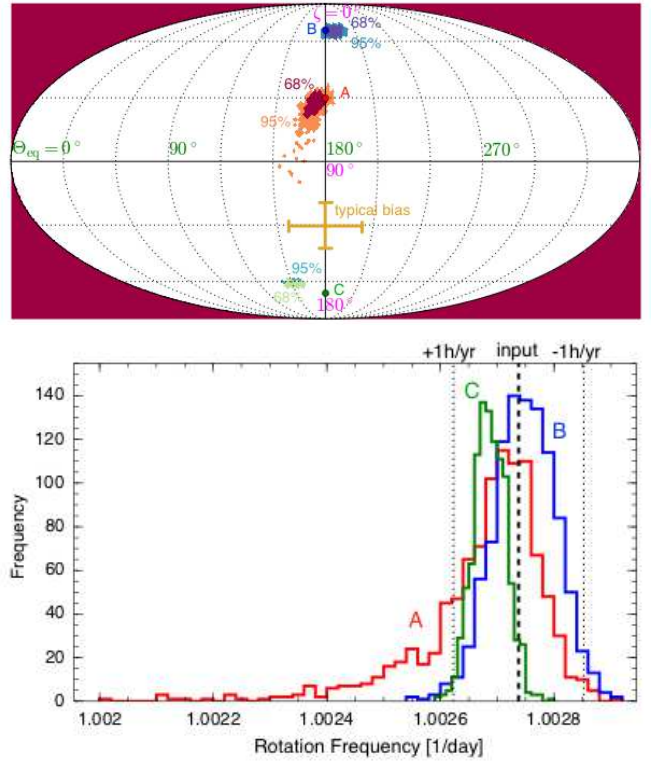


Figure 8. The areas enclosing 68 % and 90 % of the best-fit ζ and Θ_{eq} (top), and a histogram of the best-fit spin rotation frequency (bottom) for the sets of the 1000 realizations. We consider three cases: A: $\zeta = 60^\circ$ (red), B: $\zeta = 23^\circ$ (blue), and C: $\zeta = 157^\circ$ (green). In the top panel, the input value is marked by the points. The yellow cross indicates the typical bias discussed in the text. In the bottom panel, the vertical dashed line and the dotted lines indicate the input value and the one-hour errors in one year $\Delta f_{\text{spin}} \sim 1/(24 \times 365)$ [1/day].

travel time effect for a directly imaged planet in a circular orbit. The time delay is $\Delta t = -a \cos \Theta \sin i / c$, where a and c are the semimajor axis and the speed of light. The phase of the diurnal periodicity is given by

$$\psi(t) = 2\pi f_{\text{spin}}(t + \Delta t) + \text{const.} \quad (17)$$

The instantaneous frequency is expressed as

$$f_{\text{obs}} = \frac{1}{2\pi} \frac{\partial \psi}{\partial t} = f_{\text{spin}} + \epsilon_{LT}(\Theta) f_{\text{orb}} \quad (18)$$

$$\epsilon_{LT}(\Theta) = 2\pi \left(\frac{f_{\text{spin}} a}{c} \right) \sin i \sin \Theta \quad (19)$$

$$= 0.036 \left(\frac{a}{\text{au}} \right) \left(\frac{f_{\text{spin}}}{\text{day}^{-1}} \right) \sin i \sin \Theta. \quad (20)$$

The amplitude of the frequency modulation by the light-travel time effect $\Delta f = |f_{\text{obs}} - f_{\text{spin}}|$ is of the order of 10^{-4} [1/day] for $a = 1$ au, $f_{\text{spin}} = 1$ [1/day], $f_{\text{orb}} = 1/365$ [1/day]. Thus, the frequency modulation due to the light-travel time effect is two orders of magnitude smaller than the geometric effect for $a = 1$ au and a similar spin rotation rate to Earth's one. Because the thermal light also has the light-travel time effect, the light-travel time effect becomes important for the thermal emission from a long-period planet with $a > 10$ au rather than the scattered light.

4.2. Planetary Wind

The geometric effect dominates the frequency modulation for atmosphere-less planets. Indeed, atmosphere-less planets can exhibit a significant photometric variation (Fujii et al. 2014). For thin-atmosphere planets like Earth, the dynamic effect of clouds is important. The static cloud-subtracted Earth model we used in this paper implicitly assumes that the effect of clouds can be efficiently removed by the difference of two bands (Kawahara & Fujii 2011). Principal component analysis of the multi-band observation will help to make a proper combination of the bands to eliminate clouds (Cowan & Strait 2013). The validity of the assumption of the static component is of particular importance to discuss the feasibility because the seasonal changes of global planetary winds can be a possible source of the frequency modulation.

Analyzing realistic simulations of a single-band observation of a mock Earth, Pallé et al. (2008) reported slight shifts of the best-fit rotational period to shorter periods. They concluded that the variable cloud cover produced the shifts. The order of the geometric frequency modulation for Earth is $f_{\text{orb}}/f_{\text{spin}} = 0.3$ %, corresponding to the wind speed of 1.3 m/s. The seasonal change or the global difference of the wind velocity $\lesssim 1$ m/s can be comparable to the geometric effect. The possibility of the detection of the planetary wind is an interesting topic itself, and the model of the geometric frequency modulation should be still critical to extracting the modulation of the planetary winds. To investigate the effect of the global planetary wind, detailed simulations of radiative transfer with a sufficiently fine resolution of time are required. We postpone the impact of the dynamic planetary surface to a forthcoming paper using a global climate model and satellite data (Kawahara and Kodama in prep).

An application of our results to gas giants requires consideration of the differential rotation. For, instance, the zonal wind ($v \sim 100$ km/s) in Jupiter reaches ~ 1 % of the spin rotation (Vasavada & Showman 2005), which is one order of magnitude larger than $f_{\text{orb}}/f_{\text{spin}}$ even if assuming this Jupiter is located at 1 au. In this case, the differential rotation significantly affects the modulation factor. The assumption of the static surface is not valid anymore.

4.3. Comparison with inversion techniques based on the amplitude modulation

It is worth comparing our method with the traditional inversion which uses the amplitude modulation (AM-based method; Kawahara & Fujii 2010; Schwartz et al.

2015). Our method relies on the zonal inhomogeneity of the planet because the change of the longitudinal location generates the frequency modulation. As the AM-based method, Schwartz et al. (2015) showed that the longitudinal width (not the longitudinal location) and the dominant colatitude constrain the obliquity. Although the AM-based method and our techniques utilize different properties of the longitudinal kernel (i.e. width vs location), a narrow longitudinal width of the kernel increases both the amplitude and frequency modulation. In this sense, two methods extract the same information on the kernel position in the different ways.

Our approach is complementary to the AM-based technique even for practical reasons. Schwartz et al. (2015) showed that one could in principle identify the obliquity of a planet with high-precision observations of a single rotation at only two orbital phases. Our method requires full-orbit observations, whereas it works for noisy data.

The amplitude modulation does not provide a map-independent scheme for extracting planetary obliquity. Therefore, the AM-based method suffers a severe albedo-radius degeneracy. Our method does not require to solve the albedo map of the planet. The frequency modulation technique sidesteps this problem. However, our method requires the static property of the albedo map, whereas the AM-based method can in principle work for time-variable maps (Schwartz et al. 2015). Kawahara & Fujii (2011) and Fujii & Kawahara (2012) showed that the spin-orbit tomography may constrain the obliquity for the simulated Earth with cloud variability. Similarly, further simulations including the cloud variability are required to validate the frequency modulation technique for Earth-like planets.

The original spin-orbit tomography does not distinguish prograde rotation from retrograde one (i.e. ζ from $\pi - \zeta$; Kawahara & Fujii 2010). Schwartz et al. (2015) suggested that the longitudinal location of the kernel over an orbit might differentiate between the prograde and retrograde rotation. The frequency modulation is very sensitive to the difference between the prograde and retrograde rotation even for a face-on orbit, as mentioned at the end of Section 2.

Another advantage of using the frequency domain is that the information on the normalization is not required. As is apparent from the procedure of the amplitude detrending, the long-term stability over a year is not significant. Moreover, the dependence of the geometric parameters on the instantaneous frequency is intuitively comprehensible. Regarding the statistical noise, we showed the pseudo-Wigner distribution retrieved the instantaneous frequency of the data with the 100% noise compared to the standard deviation of the signal (for 2-hours). Because the typical amplitude of the variation of Earth is ~ 10 %, it corresponds to S/N ~ 10 for a 2-hour exposure. Fujii & Kawahara (2012) assumes the S/N=20 for a 4.8-hour exposure for the spin-orbit tomography corresponding to the photon limit of a 5 m telescope for a ten pc Earth. Our considered S/N is comparable to theirs.

The full inversion by the spin-orbit tomography requires a precise measurement of the spin rotation period. For instance, one can recognize the frequency modulation of the simulated light curves in the diurnal and orbital phase plane in Figure 6 of Kawahara & Fujii (2010),

which were used for the retrieval of the surface map and obliquity. However, to obtain such images, we require the precise value of the spin frequency with uncertainty below $\sim 0.2P_{\text{spin}}/P_{\text{orb}}$ (~ 5 hours error in one year). It has not been shown how to measure the spin rotation with such precision. The time-frequency analysis can provide the precise value with the uncertainty of the order of $0.1P_{\text{spin}}/P_{\text{orb}}$, which is critical even for the spin-orbit tomography.

5. SUMMARY

In this paper, we found that the axial tilt and the orbital inclination induce the frequency modulation of the apparent periodicity of the scattered light. We constructed the analytic model of the instantaneous

frequency which have three geometric parameters, the obliquity, the seasonal phase, and the spin rotation period. Fitting the instantaneous frequency extracted from the pseudo-Wigner distribution of the simulated light curve, we demonstrated that one can infer these parameters from the time-frequency analysis of the light curve of directly imaged planets. The frequency modulation provides the complementary technique to the inversion based on the amplitude modulation.

H.K. is supported Grant-in-Aid for Young Scientists (B) from Japan Society for Promotion of Science (JSPS), No.25800106. We are grateful to the referee, Nick Cowan, for many helpful suggestions, in particular, an insightful consideration of the comparison with the AM-based method.

APPENDIX

A. ANALYTIC EXPRESSIONS

The modulation factor on the maximum weighted longitude approximation is expressed as

$$\epsilon_{\zeta}(\Theta) = \frac{-\cos \zeta - \sin \zeta \cos i \sin \Delta\Theta + \cos \zeta \cos \Theta \sin i}{\cos^2 \Delta\Theta + (-\cos \zeta \sin \Delta\Theta + \cos \zeta \sin \Theta_{\text{eq}} \sin i + \sin \zeta \cos i)^2 + 2 \cos \Theta_{\text{eq}} \sin i \cos \Delta\Theta + \cos^2 \Theta_{\text{eq}} \sin^2 i}, \quad (\text{A1})$$

where $\Delta\Theta \equiv \Theta - \Theta_{\text{eq}}$.

The singular point satisfies that $|e'_{\text{M}}| = |e'_{\text{spin}}|$. In other words, the x- and y- components of equation (12) should be zero. Then, we obtain the singular point (ζ, Θ) for $\Theta_{\text{eq}} = \tilde{\Theta}_{\text{eq}}$

$$\cos(\tilde{\Theta} - \tilde{\Theta}_{\text{eq}}) = -\sin i \cos \tilde{\Theta}_{\text{eq}} \quad (\text{A2})$$

$$\tan \tilde{\zeta} = \tan i (-\sin \tilde{\Theta}_{\text{eq}} \pm \sqrt{\csc^2 i - \cos^2 \tilde{\Theta}_{\text{eq}}}). \quad (\text{A3})$$

The parameter set that satisfies the above equations corresponds to the singular point where $\hat{\phi}_{\text{M}}$ cannot be defined.

The dependence of the singular points on Θ_{eq} is shown in Figure 9. As changing Θ_{eq} , the singular point primarily runs parallel to Θ . However, when one of the singular points is passing through the inferior conjunction (denoted by IC), the inclination effect traps the singular point. Then, the interval between the pair of the singular points becomes narrow. As increasing the orbital inclination, the trapping effect becomes stronger. We also plot the null lines on which the modulation factor is zero,

$$\tan \zeta_{\text{null}} = \frac{1 + \cos \Theta \sin i}{\cos i \sin(\Theta - \Theta_{\text{eq}})}. \quad (\text{A4})$$

Thus, one can roughly imagine and understand the general feature of the modulation factor from the position of the singular points and the null line.

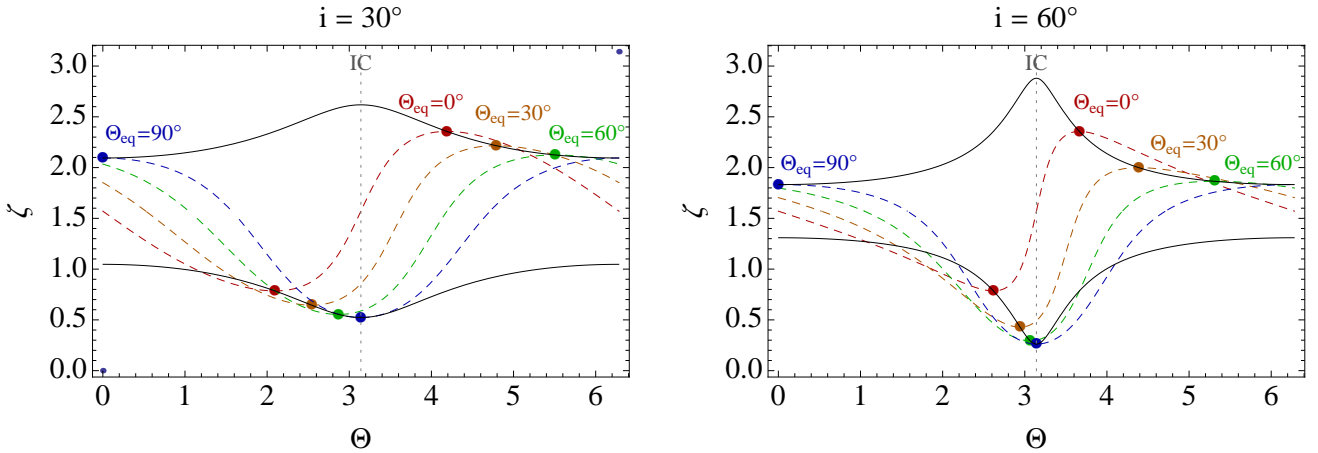


Figure 9. The singular points (marked by filled circles) and the null line ($\epsilon(\zeta, \Theta_{\text{eq}}) = 0$) as a function of Θ_{eq} (colors) for $i = 30^\circ$ and 60° . The black solid lines are trajectory of the singular point.

B. THE INSTANTANEOUS FREQUENCY EXTRACTION USING THE WIGNER DISTRIBUTION

Following Cohen (1995); Stankovic et al. (2013); Boashash (2015), we briefly summarize the Wigner distribution and the pseudo-Wigner distribution as the instantaneous frequency estimator. Let us consider the normalized analytic signal $z(t) = e^{i\psi(t)}$, where $\psi(t)$ is the instantaneous phase. The instantaneous frequency is defined by

$$f(t) = \frac{1}{2\pi} \frac{\partial \psi(t)}{\partial t}. \quad (\text{B1})$$

The ideal time-frequency representation should be expressed as

$$\rho(f, t) \propto \delta_D(f - \hat{f}(t)), \quad (\text{B2})$$

where $\delta_D(x)$ is the delta function and $\hat{f}(t)$ is the instantaneous frequency. The inverse fourier transform ($f \rightarrow \tau$) is

$$\tilde{\rho}(\tau, t) = e^{2\pi i \hat{f}(t) \tau} = \exp\left(i\tau \frac{\partial \psi(t)}{\partial t}\right). \quad (\text{B3})$$

Approximating the derivative of the instantaneous phase by

$$\frac{\partial \psi(t)}{\partial t} \approx \frac{\psi(t + \tau/2) - \psi(t - \tau/2)}{\tau}, \quad (\text{B4})$$

for a small time step τ , one obtains the Wigner distribution from the Fourier transform of the approximated $\hat{\rho}(f, \tau)$,

$$\rho(f, t) = \int_{-\infty}^{\infty} \tilde{\rho}(\tau, t) e^{-2\pi f \tau} d\tau \quad (\text{B5})$$

$$\approx \int_{-\infty}^{\infty} \exp[i\psi(t + \tau/2) - i\psi(t - \tau/2)] e^{-2\pi f \tau} d\tau \quad (\text{B6})$$

$$= \int_{-\infty}^{\infty} z(t + \tau/2) z^*(t - \tau/2) e^{-2\pi f \tau} d\tau \quad (\text{B7})$$

The pseudo-Wigner distribution is the windowed version of the Wigner distribution, which emphasizes the properties near the time of interest t and suppresses the cross term of the noise (Cohen 1995),

$$g(f, t) = \int_{-\infty}^{\infty} h(\tau) z(t + \tau/2) z^*(t - \tau/2) e^{-2\pi i f \tau} d\tau. \quad (\text{B8})$$

Because the pseudo-Wigner distribution can be expressed as the convolution of the Wigner distribution and the fourier conjugate of the window,

$$g(f, t) = \tilde{h} * \rho(f, t), \quad (\text{B9})$$

the pseudo-Wigner distribution is the smoothed version of the Wigner distribution in the frequency domain (Stankovic et al. 2013). The Hamming window is given by

$$h(\tau) = 0.54 + 0.46 \cos\left(2\pi \frac{\tau}{\omega}\right) \quad \text{for } |\tau| \leq \omega/2 \quad (\text{B10})$$

$$= 0 \quad \text{otherwise} \quad (\text{B11})$$

where ω is the window width.

C. TESTING THE PSEUDO-WIGNER DISTRIBUTION USING THE NON-UNIFORM FFT

The discrete pseudo distribution is expressed as

$$g(f, t_i) = \sum_{|m| < N/2} h[m] z[i + m] z^*[i - m] e^{-2\pi i f \tau} d\tau, \quad (\text{C1})$$

where N is the number of data. The ridge line of the pseudo-Wigner distribution is interpreted as the instantaneous frequency,

$$\hat{f}(t) = \operatorname{argmax}_{[f_i, f_j]} g(f, t), \quad (\text{C2})$$

where $[f_i, f_j]$ is the frequency range of interest.

To test our code, we generate mock data sets for a given instantaneous frequency function of $\hat{f}(t)$,

$$y_j = \cos\left(\frac{t_N}{N} \sum_{i=1}^j \frac{\hat{f}(t_i)}{2\pi}\right). \quad (\text{C3})$$

We adopt $N = 4096$ and the model of the maximum weighted longitude approximation used in Figure 6 as $\hat{f}(t)$.

As is apparent from equation (C1), the frequency is an arbitrary value (not a discrete value) under the Nyquist frequency. If using the FFT to solve equation (C1), the sampling rate of the frequency is $1/\Delta t$. The gray line in Figure 10 displays an example of the extracted instantaneous frequency using the FFT. The coarse sampling rate is due to the uniform grid. The non-uniform FFT enables us to increase the sampling rate efficiently in $O(n \log n)$ operations (Greengard & Lee 2004). The other solid lines in Figure 10 indicate the extracted instantaneous frequency using the non-uniform FFT with 4096 grids between $f = 0.972$ and 1.027 [1/day]. The computational costs of the codes with the FFT and the non-uniform FFT are on the same order.

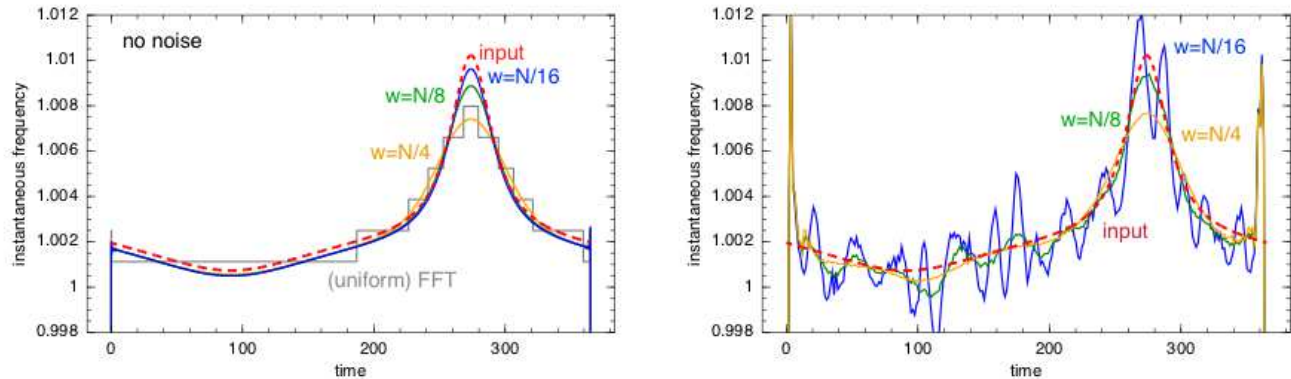


Figure 10. Left: A test of the instantaneous frequency estimation from the pseudo-Wigner distribution. The gray line uses the FFT as a Fourier-transform solver. The blue, green, and yellow curves use the non-uniform FFT with the window width of $w = N/16, N/8$, and $N/4$. The dashed curve indicates the input instantaneous frequency. Right: the extracted instantaneous frequency for the data with the 50 % noise. The curves are same to the left panel.

D. DEPENDENCE OF THE WINDOW WIDTH ON THE BIAS FOR THE NONLINEAR INSTANTANEOUS FREQUENCY AND THE NOISE SUPPRESSION

The selection of the window width affects both the bias in the frequency direction and the suppression of the noise. The blue, green, and yellow curves in the left panel of Figure 10 correspond to the extracted instantaneous frequency using $w = N/16, N/8$ and $N/4$, where $w = \omega N/t_N$. In the left panel, we do not add any additional noise. As decreasing the window size, the bias at a nonlinear instantaneous frequency point becomes smaller. However, there is the trade-off relation between the frequency bias and the noise suppression (or frequency resolution). Figure 10 shows the extracted instantaneous frequency using the same window sizes to the left panel for the data with additional noises (50 % of the standard deviation of the signal). The extracted instantaneous frequency with a smaller window exhibits higher noises (or poor resolution of the instantaneous frequency). Thus, the adequate size of the window depends on the noise level of the data.

For the highly non-linear instantaneous frequency, the adaptive algorithm that determines the appropriate window size as a function of time was proposed (Section 5 of Stankovic et al. 2013). We tried to use the adaptive algorithm and found that the adaptive algorithm chooses smaller window at the peak of the instantaneous frequency. However, there are other artifacts from the adaptive algorithm, and our data is not likely to be highly nonlinear. Therefore, we decide to use a constant window size for simplicity in this paper.

REFERENCES

- Agnor, C. B., Canup, R. M., & Levison, H. F. 1999, *Icarus*, 142, 219
 Agol, E., Cowan, N. B., Knutson, H. A., et al. 2010, *ApJ*, 721, 1861
 Barnes, J. W., & Fortney, J. J. 2003, *ApJ*, 588, 545
 Barucci, M. A., Capria, M. T., Harris, A. W., & Fulchignoni, M. 1989, *Icarus*, 78, 311
 Bezanson, J., Edelman, A., Karpinski, S., & Shah, V. B. 2014, ArXiv e-prints, arXiv:1411.1607
 Boashash, B. 2015, *Time-Frequency Signal Analysis and Processing*, 2nd Edition A Comprehensive Reference (Elsevier)
 Borkovits, T., Hajdu, T., Sztakovics, J., et al. 2016, *MNRAS*, 455, 4136
 Carter, J. A., & Winn, J. N. 2010, *ApJ*, 709, 1219
 Chambers, J. E. 2001, *Icarus*, 152, 205
 Cohen, L. 1995, *Time Frequency Analysis: Theory and Applications*, 1st Edition (Prentice hall)
 Conroy, K. E., Prša, A., Stassun, K. G., et al. 2014, *AJ*, 147, 45
 Cowan, N. B., & Strait, T. E. 2013, *ApJ*, 765, L17
 Cowan, N. B., Agol, E., Meadows, V. S., et al. 2009, *ApJ*, 700, 915
 Cowan, N. B., Robinson, T., Livengood, T. A., et al. 2011, *ApJ*, 731, 76
 Ford, E. B., Seager, S., & Turner, E. L. 2001, *Nature*, 412, 885
 Fujii, Y., & Kawahara, H. 2012, *ApJ*, 755, 101
 Fujii, Y., Kawahara, H., Suto, Y., et al. 2011, *ApJ*, 738, 184

- . 2010, *ApJ*, 715, 866
- Fujii, Y., Kimura, J., Dohm, J., & Ohtake, M. 2014, *Astrobiology*, 14, 753
- Górski, K. M., Hivon, E., Banday, A. J., et al. 2005, *ApJ*, 622, 759
- Greengard, L., & Lee, J.-Y. 2004, *SIAM Review*, 46, 443
- Kawahara, H. 2012, *ApJ*, 760, L13
- Kawahara, H., & Fujii, Y. 2010, *ApJ*, 720, 1333
- . 2011, *ApJ*, 739, L62
- Kokubo, E., & Ida, S. 2007, *ApJ*, 671, 2082
- Markwardt, C. B. 2009, in *Astronomical Society of the Pacific Conference Series*, Vol. 411, *Astronomical Data Analysis Software and Systems XVIII*, ed. D. A. Bohlender, D. Durand, & P. Dowler, 251
- Masuda, K., Uehara, S., & Kawahara, H. 2015, *ApJ*, 806, L37
- Nikolov, N., & Sainsbury-Martinez, F. 2015, *ApJ*, 808, 57
- Oakley, P. H. H., & Cash, W. 2009, *ApJ*, 700, 1428
- Pallé, E., Ford, E. B., Seager, S., Montañés-Rodríguez, P., & Vazquez, M. 2008, *ApJ*, 676, 1319
- Rappaport, S., Deck, K., Levine, A., et al. 2013, *ApJ*, 768, 33
- Russell, H. N. 1906, *ApJ*, 24, 1
- Schwartz, J. C., Sekowski, C., Haggard, H. M., Pallé, E., & Cowan, N. B. 2015, *ArXiv e-prints*, arXiv:1511.05152
- Seager, S., & Hui, L. 2002, *ApJ*, 574, 1004
- Shibahashi, H., & Kurtz, D. W. 2012, *MNRAS*, 422, 738
- Stankovic, L., Daković, M., & Thayaparan, T. 2013, *Time-frequency signal analysis with applications* (Artech House)
- Vasavada, A. R., & Showman, A. P. 2005, *Reports on Progress in Physics*, 68, 1935
- Visser, P. M., & van de Bult, F. J. 2015, *A&A*, 579, A21
- Williams, D. M., & Kasting, J. F. 1997, *Icarus*, 129, 254
- Williams, D. M., & Pollard, D. 2003, *International Journal of Astrobiology*, 2, 1